Damage detection on antarctic ice shelves using the normalised radon transform

Izeboud, M.; Lhermitte, S.L.M.

Important note
To cite this publication, please use the final published version (if applicable).
Please check the document version above.

Damage detection on antarctic ice shelves using the normalised radon transform

Maaike Izeboud [a,*], Stef Lhermitte [a,b]

[a] *Delft University of Technology, Stevinweg 1, Delft, The Netherlands*
[b] *KU Leuven, Celestijnenlaan 200E, Leuven, Belgium*

ARTICLE INFO

ABSTRACT

Areas of structural damage mechanically weaken Antarctic ice shelves. This potentially preconditions ice shelves for disintegration and enhanced grounding line retreat. The development of damage and its feedback on marine ice sheet dynamics has been identified as key to future ice shelf stability and sea level contributions from Antarctica. However, it is one of the least understood processes that impact ice shelf instability since quantifying damage efficiently and accurately is a challenging task. Challenges relate to the complex surface of Antarctica, variations in viewing-illumination geometry, snow or cloud cover and variable signal-to-noise levels in satellite imagery. Therefore, automated damage assessment approaches require careful pre- and post-processing, lacking the option to be applied to wider spatiotemporal domains. Simultaneously, studies that use manual mapping are usually limited due to the effort required for extensive mapping, which either results in a limited spatial domain or the use of low resolution data.

This study proposes the NormalisEd Radon transform Damage detection (NeRD) method to detect damage features and their orientations from multi-source satellite imagery. NeRD performs robust, high resolution, large-scale damage assessments. NeRD is applied to the ice shelves in the Amundsen Sea Embayment (ASE) and validated with both manually labelled and existing fracture maps. Validation shows that NeRD detects damage with high recall and provides an accurate physical representation of multi-scale damage features and their orientation. Sensitivity analyses indicate NeRD is robust to different resolution parameter settings. NeRD consistently detects damage for different data sources ranging from optical Landsat 7/8 and Sentinel-2 optical to Synthetic Aperture Radar Sentinel-1 data. Therefore, NeRD paves the way for synergistic multi-source damage detection that overcomes remaining limitations from individual sources. Results show varying damage patterns on the ice shelves in the ASE area in austral summer 2020–2021, with most damage located on the Pine Island, Crosson and Thwaites ice shelves. We show a damage increase on the Pine Island ice shelf between 2013–2019, and display advection and rotation of crevasses. The detected damage orientation can provide insight in the type of crevasse opening mode and the development of damage over time. The damage maps produced with NeRD can help evaluate ice sheet models or machine learning approaches, improving our understanding of damage evolution.

1. Introduction

Antarctic ice shelves modulate grounded ice flow through buttressing. Their weakening or disintegration is crucial for the timing and magnitude of grounded ice loss and onset of instabilities (Sun et al., 2017; Benn and Åström, 2018; Vieli et al., 2007; Albrecht and Levermann, 2012), and thereby for the sea level contributions from Antarctica (Fox-Kemper et al., 2021). The development of damage areas in the shear zones of an ice shelf are first signs of structural weakening. Damage areas typically consist of highly crevassed areas, rifts and open fractures containing dense ice mélange (Lhermitte et al., 2020; Borstad et al., 2012). The development of damage in the shear zones of an ice shelf can result in further speedup, shearing and weakening, hence promoting additional damage development. This feedback potentially preconditions ice shelves for disintegration and enhanced grounding line retreat (Lhermitte et al., 2020). For example, damage has been considered key for the ice shelf collapse of Larsen B and the retreat of Pine Island Glacier and Thwaites Glacier (Glasser and Scambos, 2008; Borstad et al., 2012). Although this damage feedback has been identified as key to future ice shelf stability, it is one of the least understood processes in marine ice sheet dynamics.

Remote sensing data provides the possibility to detect fractures and damage areas across Antarctic ice shelves and the ice sheet. Where laser altimetry is used to map vertical properties, quantifying the continuous distribution of fractures in the horizontal dimension remains unsolved (Wang et al., 2021; Herzfeld et al., 2021; Li et al., 2021). Assessing horizontal properties of fractures and damage from satellite imagery can be a complicated task due to three major challenges. Firstly, there are morphological similarities between full-thickness rifts, surface expressions of basal fractures, and flow lines (Luckman et al., 2012; McGrath et al., 2012a) that are difficult to distinguish (Colgan et al., 2016; Ely and Clark, 2016). As a result, for practical purposes, fractures are often mapped manually. Secondly, the spatial resolution of available data and the research focus of the individual studies determines the size and scale of the features that are resolved. Damage comes in all shapes and sizes: from small surface crevasses in densely crevassed fields to full-thickness rifts near the ice front of multiple kilometres long, to the complex and irregularly shaped ice mélange in damaged shear zones. Thirdly, similar damage may appear different in different images due to changing illumination or viewing conditions, the complex surface of the Antarctic, snow or cloud cover, or variable signal-to-noise levels (speckle) in SAR imagery (Colgan et al., 2016). These challenges imply that most studies in practice either perform an extensive manual mapping of fine resolution features, such as Scambos et al. (2009), Kaluzienski et al. (2019) or focus on large-scale linear rifts in data with coarser spatial resolution (e.g., MODIS) that cannot capture small scale features (Glasser and Scambos, 2008; Lai et al., 2020).

Previous studies such as Bhardwaj et al. (2016) and Colgan et al. (2011) have developed approaches to perform fine-resolution crevasse or crevasse field detection on optical data, but these approaches are not easily applied on a large spatiotemporal scale. Bhardwaj et al. (2016) used band ratios from pan-sharpened Landsat 8 optical and thermal bands to create a fine resolution (15 m) but small spatial crevasse map, covering 4 km². Colgan et al. (2011) manually digitised crevasse fields after convolving a high-quality panchromatic aerial photograph (2 m resolution) with a Roberts cross-edge detector. Both studies were limited to two dates on a single glacier. Alternatively, a first Antarctic-wide fracture map has been developed by Lai et al. (2020) using a deep Convolutional Neural Network (CNN). This CNN, however, was trained on manually labelled large-scale rifts and applied on a relatively coarse resolution MODIS mosaic (125 m), resulting in the loss of fine spatial detail of the damage features.

The Radon transform was proposed as an alternative, more robust approach to detect crevasses (Gong et al., 2018). The Radon transform can detect both linear fractures and more complex patterns of heavily damaged areas, where other edge detection methods fail or require extensive processing (Bhardwaj et al., 2016; Colgan et al., 2011; Roberts et al., 2013; Gong et al., 2018). The Radon transform was previously applied to both SAR and optical satellite data for flow line detection (Roberts et al., 2013) and crevasse detection (Gong et al., 2018). This dual application moreover highlights the potential to combine different data sources in a new detection approach, overcoming limitations from each individual source. Furthermore, the Radon transform can detect both feature orientation and feature signal strength, allowing insight in crevasse rotation and advection over time. One drawback of the Radon transform as damage detector developed by Gong et al. (2018), however, is the lack of consistency to quantify damage. The current method depends on the intensity of the (grey-scale) image pixels which often varies in space and time and even depends on the cut-out windows of the Radon transform. Different illumination conditions, look-angles, and sensors affect the image intensity, resulting in different crevasse signal values. These issues limit the application of the Radon transform as a method for generalised, automated damage assessments.

In this study we propose a novel method that builds upon the Radon transform method of Gong et al. (2018) to allow a generalised damage assessment. To this end, we have developed the NormalisEd Radon transform Damage detection (NeRD) method (Section 2) which can be applied directly to multiple satellite data sources across spatial or temporal domains, without requiring additional pre- or post-processing. This includes optical and SAR data from Sentinel-1, Sentinel-2 and Landsat 7/8. We apply NeRD to ice shelves in the Amundsen Sea Embayment (Section 3), and test the method for different parameter settings related to spatial resolution and data source (Section 4). The results are validated by comparing with a manually labelled damage map of multi-scale damage features, and with the existing CNN fracture map of Lai et al. (2020). In Section 5 we display the damage detection product, showing constructed damage maps for the ASE area including damage signal and damage orientation, the performance and evaluation of the NeRD method, and finally its application on a time series of the Pine Island Ice Shelf satellite data.

2. NormalisEd Radon transform Damage detection (NeRD)

The NormalisEd Radon transform Damage (NeRD) detection method builds upon the method of Gong et al. (2018) and Altena (2018), which were initially based upon the work of Roberts et al. (2013). NeRD is intended to be a robust and generalised, one-size-fits-all method that can be applied across image sources and results in a consistent, quantitative damage detection product.

Roberts et al. (2013) used the Radon transform to detect flow lines and their orientations on the Amery ice shelf using RADARSAT data, whereas Gong et al. (2018) used the Radon transform to detect crevasses and their orientations on the Austfonna ice cap (Svalbard) from Landsat 8 data. Both used a similar approach, consisting of: (i) pre-process the image with a Laplacian filter to enhance edge contrast and remove noise, (ii) extract cut-out windows from the image, (iii) apply the Radon transform to the cut-out windows, (iv) extract dominant feature signal strength and dominant feature orientation for every window, and finally, (v) post-processing. However, there are two issues in this approach that hinder a quantitative and consistent interpretation of the feature signals.

The first issue stems from Radon transform algorithm itself, and how it extracts the feature signal. The Radon transform is a line-detection algorithm that projects the image (or cut-out window) intensity along a radial line oriented at a specific angle (Oppenheim and Willsky, 1996). See for a schematic example Fig. 1, where the line integral is displayed for two example projection angles. The standard deviation or variance of this line-integral indicates the level of contrast within the window at each angle and the maximum standard deviation across all angles is used to extract a feature signal and orientation (Roberts et al., 2013; Altena, 2018).

The drawback of the classical Radon transform is that the feature signal retrieved from the Radon transform line-integral is dependent on the pixels in the cut-out window. This manifests in three problems. First, the feature signal value depends on the number of pixels in each cut-out window. This results in higher signal values for larger windows. Second, the signal value is dependent on the average pixel intensity values, yielding higher signal values for brighter images. Third, the Radon transform returns false signals for uniform data. Because of these problems, the results of the classical Radon transform are inconsistent between different images or cut-out windows as the signal value of the Radon transform is relative to each processing window instead of a global value across the image. This limits a generalised implementation of damage detection.

In the NeRD method we propose to solve these three problems by normalisation of the Radon transform. Normalisation makes the Radon signal value independent of the number of pixels in the window, and unbiased to shifts in pixel intensity values. The false signals are then removed as a result, solving all three problems. See for example Fig. 1a: the Radon transform without normalisation shows a varying line integral over the two projection axis for a uniform window. This means that the variance is non-null and yields a false signal. The
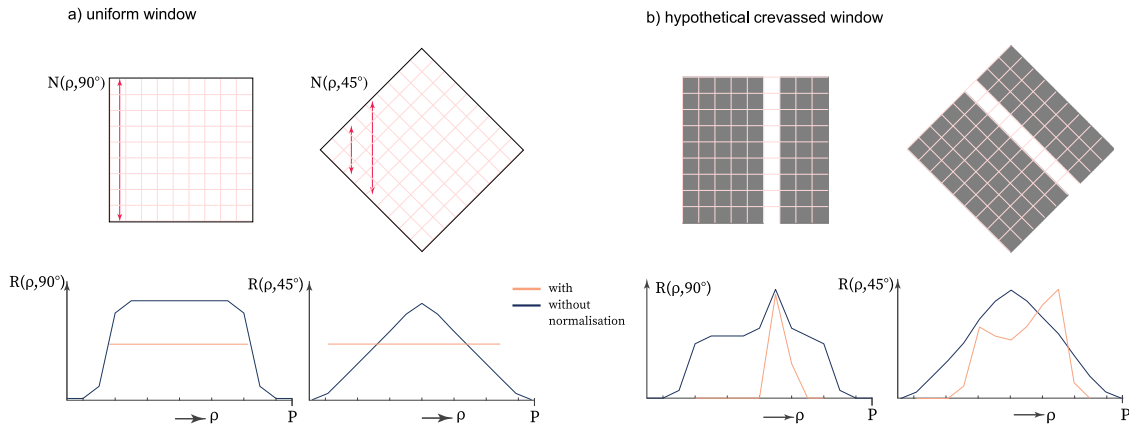
Fig. 1. Concept of the (Normalised) Radon transform for two idealised image cut-out windows, (a) a uniform window (white value 1) without any variation in pixel values, (b) a window with a simplified representation of a crevasse (grey value 0.5 and white value 1). The figure shows the line-integral calculated for different projection axis ρ at angle θ, with (orange) and without (blue) normalisation. $R(\rho, \theta)$ is shown here for $\theta = 45°$ and $\theta = 90°$. N denotes the number of pixels in the line integral for every projection, P denotes the number of steps within the domain of the projection axis. (For interpretation of the references to colour in this figure legend, the reader is referred to the web version of this article.)

normalised Radon transform, however, is a flat line, which (correctly) returns no signal. With NeRD, the damage signal value depends only on the contrast of a linear feature in the window, rather than on the size of the feature or window. Therefore, NeRD yields a consistent value that can be interpreted across all windows and between different images. Although the signal value is independent of the number of pixels in the window, it should be noted that the window size still determines which features can be detected. If the window is too large/small to reveal the features to be detected, it will not work and NERD is consequently not completely independent of the window size. A proof-of-concept of implementing the normalisation step is provided in Section 2.3. Here further detail and examples are provided to illustrate how the three problems are solved.

The second issue of the Radon transform as applied by Roberts et al. (2013) and Gong et al. (2018) is introduced in the pre-processing of the image using an edge-enhancement Laplacian filter. This filter re-scales the grey-scale input image into binary black and white values and, consequently, maximises all edge-like surface features and removes noise. This potentially includes maximising surface roughness features such as snow dunes or sastrugi that should not be detected as damage. Additionally, the use of the Laplacian filter reduces all existing contrast gradations into binary 0/1 values. Consequently, the Radon transform is no longer able to distinguish between features that display different contrast strengths and provide a quantitative measure of strength of the damage signal. This quantitative measure can however be potentially useful to discriminate between damage features as we expect that strong and prominent contrasts correspond to large damage features, such as a rifts, while low contrast features presumably correspond to smaller scale damage features, such as surface crevasses. Similarly, an opening crevasse will show changes in contrast over time. As a solution to this issue we remove the use of a Laplacian filter as a pre-processing step and replace it with a post-processing step that removes noise from the output by setting a minimum signal threshold. This allows NeRD to detect continuous, quantitative damage signals without contaminating the product with noise.

In summary, the presented NeRD method consists of the following steps: (i) create cut-out windows from the image, (ii) apply the Normalised Radon transform to these windows, (iii) extract dominant feature signal strength and orientation for every window, (iv) quantify the damage signal value by removing noise from the signal and (v) post-processing. In the NeRD post-processing step we remove image borders and rock outcrops from the detection product.

2.1. The normalised Radon transform

The Radon transform is the line-integral of the image (or cut-out window) intensity along a projection axis (ρ) oriented at a specific angle (θ) (Oppenheim and Willsky, 1996). An example is shown in Fig. 1 for rotation $\theta = 90°$ and $\theta = 45°$. By repeating the line-integration for axes oriented at all angles $\theta = 0°$ to $\theta = 180°$, a 2-D feature space $R(\rho, \theta)$ is constructed. In NeRD, a normalisation step similar to Öznergiz et al. (2014) is added to the Radon transform by normalising the line-integral over each projected axis ρ to the number of pixels $N(\rho, \theta)$ within the integral. The Normalised Radon transform is computed as:

$$R_{norm}(\rho, \theta) = \frac{1}{N(\rho, \theta)} \sum_x \sum_y I(x, y)\delta(\rho - (x \cos \theta + y \sin \theta)) \quad (1)$$

where $I(x, y)$ denotes the value of the image intensity at (x, y) coordinates, and δ is the delta Dirac function (Oppenheim and Willsky, 1996; Öznergiz et al., 2014). The range of the transform coordinates is a half circle ($0 \leq \theta < \pi$). The result of the transform is a 2-D feature space at different azimuthal orientations (θ) as can be seen in Fig. 2 panels a2–e2.

The variability of $R_{norm}(\rho, \theta)$ indicates the level of contrast for every projection axis. This maximises on the cross-section of narrow linear features, i.e. when the feature is perpendicular to the projection axis. This shows in the line-integral as a sharp narrow peak, as is illustrated in Fig. 1b. The signal response (σ) is therefore calculated as the standard deviation of R_{norm} for all projection angles, which is then filtered with a running median filter of size two ($\Delta = 1°$) to remove noise (Gong et al., 2018):

$$s(\theta) = \sqrt{\frac{1}{P-1} \sum_{i=1}^{P} \left(R_{norm}(\rho, \theta) - \overline{R_{norm}} \right)^2}, \quad (2)$$

$$\sigma(\theta) = median\{s(\theta - \Delta), \dots, s(\theta + \Delta)\}. \quad (3)$$

Here P denotes the number of steps within the domain of the projection axis ρ. For $\theta = [0, 90, 180]$, P is equal to the width of the window. For $\theta = 45°$, P is equal to the diagonal of the window.

The signal response (σ) is shown in Fig. 2 panels a3–e3. The projection angle with the maximum signal response $\sigma(\theta)$ is extracted as the dominant crevasse signal value of the window:

$$\sigma_{crev} = max(\sigma(\theta)). \quad (4)$$

2.2. Damage signal and orientation

After extracting the crevasse signal (σ_{crev}) for every window, σ_{crev} is translated into a damage signal ($\hat{D}$). A signal $\sigma(\theta) > 0$ will be found
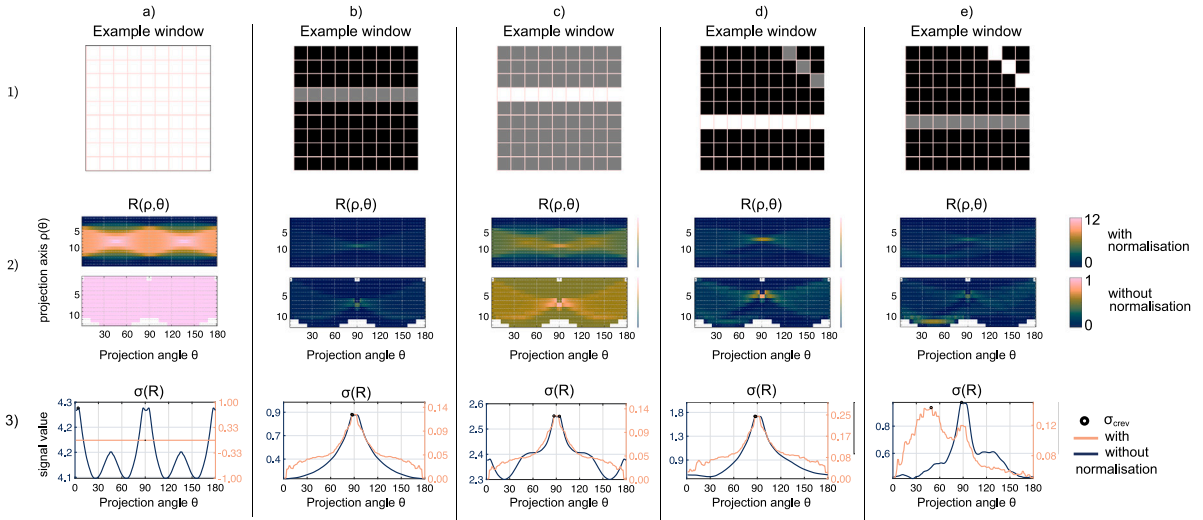
Fig. 2. Idealised scenario's to illustrate the differences between the Radon transform with and without normalisation. Panel a–e represent different scenario's to which the Radon transform is applied: a1–e1 show an idealised window with a hypothetical crevasse, a2–e2 show the corresponding 2-D feature space $R(\rho,\theta)$ without and with normalisation (respectively top and bottom), and a3–e3 the signal response $\sigma(\theta)$ with and without normalisation — from which σ_{crev} is extracted (black dot).

by NeRD for any window with non-uniform pixel values. This includes noisy windows that contain no damage feature and that should be removed from the damage detection product. We therefore apply a crevasse signal threshold τ_{crev} to remove the noise background signal. The damage signal $\hat{D}$ is then defined as:

$$\hat{D} = \begin{cases} \sigma_{crev} - \tau_{crev}, & \text{if } \sigma_{crev} \geq \tau_{crev}, \\ 0, & \text{otherwise.} \end{cases} \tag{5}$$

The threshold τ_{crev} represents the 'noisy signal value'. τ_{crev} is calculated separately, and varies slightly according to the data source and window size that σ_{crev} is calculated on (further detail in Section 4.2.1). Because R_{norm} values are between 0 and 1 the standard deviation and thus σ_{crev} has a maximum value of 0.5 (Shalom and Mandeville, 1982). Consequently, $\hat{D} \in [0, 0.5 - \tau_{crev}]$, where value 0 represents intact ice. The maximum value for $\hat{D}$ is reached at maximum black/white contrast values. This can occur for full-depth rifts with ice/ocean contrasts but might also occur for surface crevasses with dark shadows. $\hat{D}$ therefore does not directly present mechanical degradation of the ice such as the often used (depth integrated) isotropic scalar damage in continuous damage mechanics (CDM) modelling (Borstad et al., 2012, 2013, 2016; Sun et al., 2017).

The projection angle θ for which the maximum crevasse signal occurs is rotated 90° to represent the accompanying damage orientation $\alpha_{\hat{D}}$:

$$\alpha_{\hat{D}} = \theta - 90°. \tag{6}$$

The interpretation of $\alpha_{\hat{D}}$ is more intuitive to interpret after a 90° rotation, as it then references the orientation of longitudinal direction of the feature with respect to the image horizontal. For example in Fig. 1b, σ maximises at $\theta = 90°$. At this angle, the line-integral results in the most pronounced sharp peak and thus has the largest signal response $\sigma(\theta)$. The resulting damage orientation will be $\alpha_{\hat{D}} = 0$ which intuitively corresponds to the horizontal line of the window. More examples and explanations are provided in Section 2.3.

2.3. Proof of concept

In this section we illustrate that normalisation of the Radon transform solves the three issues mentioned earlier: (i) it removes false signals, (ii) the signal value is independent of the number of pixels in the window, and (iii) the signal value is unbiased to average pixel

intensity values. Consequently, NeRD solely depends on the contrast of the linear feature.

To illustrate the differences, we performed the Radon transform with and without normalisation on a set of idealised windows that portray simplified crevasses. The results are displayed in Fig. 2, where every panel shows an idealised window in row 1, its 2-D feature space $R(\rho,\theta)$ with and without normalisation in row 2, and its signal response $\sigma(R)$ with and without normalisation in row 3 — from which σ_{crev} is extracted.

Panel Fig. 2-a1 displays a uniform window with grey-scale values of 1. This example best illustrates the effect the number of pixels (N) have on the Radon transform. Without normalisation, $R(\rho,\theta)$ changes for different projection angles (panel a2), yielding $\sigma(\theta) \neq 0$ (panel a3). False local maxima signals appear at 0°, 45°, 90°, 135° and 180° (panel a3), and the maximum signal corresponds to $\theta = 0°, 90°$ or 180°. The false signals are the result of the changing length of the projection axis for different rotation values as the projection axis varies between the window width ($\theta = 0°, 90°$ or 180°) and window diagonal ($\theta = 45°$ or 135°). Consequently, for shorter projection axis, ρ is padded with zeros to fill the 2-D space of $R(\rho,\theta)$ to maximum length P. This padding creates an artificial jump in $R(\rho,\theta)$ values that results in false signals (see also Fig. 1a). Now, with normalisation, padding with zeros and the artificial jump is unnecessary as P is allowed to vary with each projection angle. Therefore, a uniform window will result in $R_{norm} = 1$ and an extracted signal $\sigma_{crev} = 0$.

Panels Fig. 2b–c illustrate that the Normalised Radon transform is independent of the average pixel intensity values. These examples show the same feature, with the same contrast value of 0.5: a background pixel intensity 0/0.5 and line intensity of 0.5/1, for panels b1 and c1 respectively. In these examples, the values of R_{norm} and σ_{crev} are identical despite the shift in the average intensity values: $\sigma_{crev} = 0.12$. Without normalisation this is not the case: the signal response changes from $\sigma_{crev} \approx 0.9$ to $\sigma_{crev} \approx 2.55$ (panels b3–c3).

Finally, Fig. 2d–e shows that the Radon Transform without normalisation gives more weight to long linear features, while the Normalised Radon transform puts more weight on linear features with high contrast values. This effect is illustrated in panels d1/e1 which show a long, high/low-contrast linear feature at $\theta = 90°$ and a short, low/high-contrast feature at angle $\theta = 45°$, respectively. In window d1 the extracted crevasse orientation is $\theta = 90°$ ($\alpha_{\hat{D}} = 0°$) with and without normalisation, corresponding to the long, high-contrast feature. There is a difference in the value for σ_{crev} (panel d3), though. For window e1, however, the extracted crevasse orientation differ with or without

normalisation. Without normalisation, the dominant signal remains at $\theta = 90°$, here corresponding to the long, *low*-contrast feature, whereas the Normalised Radon transform yields $\theta = 45°$, corresponding to the short, *high*-contrast feature. This indicates that Normalised Radon transform gives more weight to feature contrast than length.

3. Study area and data

3.1. Study area

We applied the proposed NeRD method to the ice shelves in the Amundsen Sea Embayment in Antarctica. We considered all ice shelves between $100°–125°$ West, which contains the Abbot, Cosgrove, Pine Island, Thwaites, Crosson, Dotson and Getz ice shelves.

The Amundsen Sea Embayment in West Antarctica is currently the largest contributor to sea-level rise (Pattyn and Morlighem, 2020). Most mass loss in the past decades is from Pine Island and Thwaites Glacier (Arndt et al., 2018; Meredith et al., 2019). Crosson and Dotson are two of the most rapidly changing outlets in West Antarctica (Lilien et al., 2018), but Thwaites Glacier is undergoing the largest changes of any ice–ocean system in Antarctica (Miles et al., 2021). The ice flow acceleration and ice shelf thinning is associated to grounding-line retreat (Pattyn and Morlighem, 2020; Arndt et al., 2018). Damage on these ice shelves has been considered key to their retreat (Glasser and Scambos, 2008; Borstad et al., 2012; Lilien et al., 2018; Lhermitte et al., 2020). Also Getz ice shelf was shown to be accelerating (Chuter et al., 2017).

Given the presence of multiple fast changing, fast flowing and heavily damaged ice shelves in the Amundsen Sea Embayment, assessing the amount of damage in this area is of primary interest to improve our understanding of the link between damage, mechanical weakening and ice shelf instability.

3.2. Satellite imagery

To evaluate the NeRD method, we applied it to a variety of satellite data sources ranging from Sentinel-2 Level-1C, Landsat 7 and Landsat 8 Collection 1 Tier 2 Top of Atmosphere Reflectance images and Syntetic Aperture Radar (SAR) Sentinel-1 Ground Range Detected images. All images were pre-processed in Google Earth Engine (Gorelick et al., 2017) and were exported at the same 30 m resolution as images from the Landsat series in WGS 84 Antarctic polar Stereographic projection (EPSG:3031). Sentinel-1 (10 m) and Sentinel-2 (10 m and 20 m) images were re-sampled using the nearest neighbour method. The MEaSUREs Antarctic ice shelf boundaries dataset of Rignot et al. (2016) was used to select satellite imagery over the ice shelves in the study area, and later to plot the grounding line on the spatial figures.

The satellite imagery was pre-processed in two ways to obtain a single, frame-filling image for every austral summer (December, January, February; DJF). Firstly, the optical satellite images were obtained by constructing a *median composite* image. This consisted of the following steps: subsetting the image collection to DJF data only, filtering for cloud cover (<20%) and compositing into median annual DJF composites of the Red (R), Green (G), Blue (B) reflectance bands. Calculating the DJF median of the image collection introduces a resolution loss of surface features due to a blurring effect as a result of glacier displacement. Especially fast flowing ice shelves, such as Pine Island, Thwaites and Crosson, show significant ice displacement throughout one austral summer with velocities up to 5 km/year (Gardner et al., 2019; Mouginot et al., 2017a). Shortening the image composite interval would reduce this blurring effect, but severely limits the available images, often leaving large gaps in the data. To show the capability of NeRD as an automated approach, applied to automatically retrieved data of sufficient quality, it was opted in this study to work with optical DJF median composites rather than monthly composites or individual scenes.

Secondly, SAR images were obtained by constructing a *spatial mosaic* image, stitching individual scene together until the export frame was filled. SAR data does not require filtering for cloud cover, and thus a qualitative image for a chosen period can be generated automatically without compositing. The SAR images were not filtered to remove speckle noise, as a noise removal step is already included in the NeRD method. The Sentinel-1 collection was filtered to only include HH polarisation images of Interferometric Wide Swath instrument mode and descending orbit in the defined DJF period.

Supplementary Figure 1 displays the retrieved Sentinel-2 median composite images for DJF 2020–2021 for Pine Island, Thwaites, Crosson and Getz ice shelves. Supplementary Table 1 provides an overview of image median composites and spatial mosaics used in this study for each satellite source.

4. Methods

NeRD is intended to be a generalised, one-size-fits-all method: a method that can be applied to images from different spatial or temporal domains and yield results that can be compared. Therefore, we first performed sensitivity tests to show the robustness of NeRD (Section 4.1) to its inputs before applying NeRD to the Amundsen Sea Embayment study area (Section 4.2) and validating the results (Section 4.3). In a final step we have applied NeRD to a timeseries of imagery over the Pine Island Glacier to analyse its temporal consistency.

4.1. Sensitivity analysis

The sensitivity of NeRD to its parameter settings and input was tested in two experiments. The first 'resolution sensitivity' experiment focuses on the choice of processing window size in combination with the image pixel resolution. The second 'sensor sensitivity' experiment considers the sensitivity of the result to different data inputs. For this we consider both the choice of spectral bands in optical data, as well as the difference between optical and SAR data.

4.1.1. Resolution sensitivity

First, the sensitivity of the NeRD method to the choice of window size was tested. The choice of window size is a compromise between desired high output resolution, and accurate feature detection. On the one hand feature detection in small window sizes yield high output resolution. On the other hand, feature detection in small windows is more susceptible to noise because the linearity of a feature typically is less pronounced in small windows where linear features have lower length to width ratios. Since the high length to width ratios of linear features determines the signal value in R_{norm}, it will result in lower damage signals. Consider for example an open rift of 100 m wide and 10 km long. A small window of 10×10 m can 'fall into' the rift and miss its detection. Detection is possible if the small window covers the edge of the rift, and the edge is discernible as a linear feature from surrounding surface irregularities (noise) within the window. A larger window improves the confidence of feature detection over noise (Roberts et al., 2013) as a larger window size (e.g. 1 km × 1 km) spans the rifts opening and clearly shows the orientation of the rift. A drawback of this larger window size is that other features which are present in the window might be overridden by the large rift. The output of larger window sizes therefore potentially misses valuable spatial variations. As such, a balanced choice of window size relative to feature size is essential. Therefore, to test the effects of window size on the detected NeRD damage we performed a sensitivity experiment by varying the window sizes between 10×10 and 25×25 pixels, implying window sizes of 300×300 and 750×750 m, respectively. An example for these two window sizes is shown in Fig. 3a and b.

Second, the sensitivity of the NeRD method to the image pixel resolution was tested. The resolution of the image mainly determines the minimum feature size that can be resolved, but also affects the
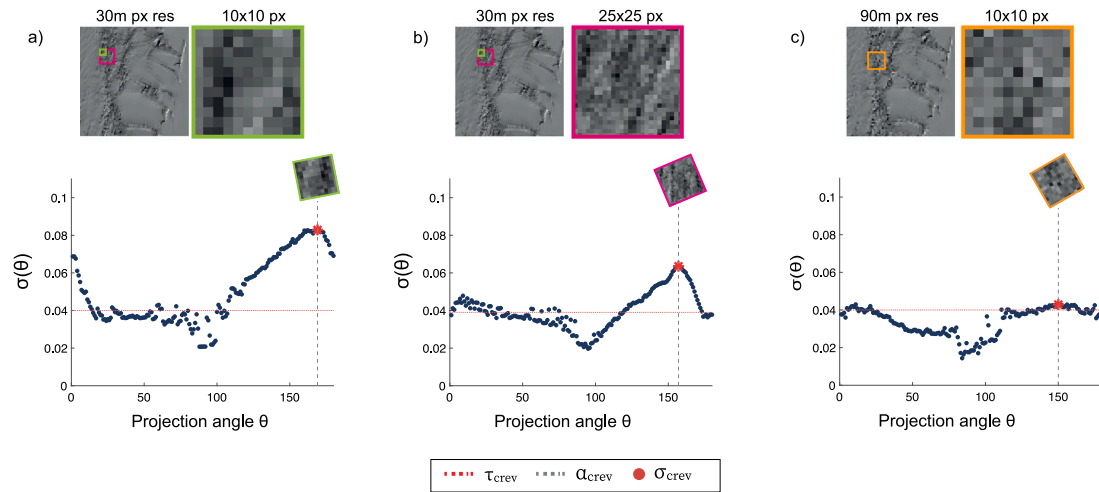
Fig. 3. Example of NeRD applied to different windows of a Sentinel-2 RGB median composite of DJF 2019–2020, zoomed in to the western shear zone of Pine Island Ice Shelf. The image has been converted to a greyscale image with values between 0–1. The top row shows the selection of (a) a 10×10 (green) and (b) 25×25 (magenta) pixel windows from the image with 30 m pixel resolution, and (c) a 10×10 (orange) pixel window from a down-sampled image to 90 m pixel resolution. The bottom row shows the standard deviation $\sigma(\theta)$ of the normalised radon transform line integral at different projection angles θ. The resulting crevasse signal σ_{crev} at angle θ are denoted with a red dot and grey dashed line. The crevasse signal threshold τ_{crev} is shown as the red dashed line. (For interpretation of the references to colour in this figure legend, the reader is referred to the web version of this article.)

contrast of features. Since wide linear features (e.g. rifts) can be located in a multitude of pixels in high spatial resolution imagery, the contrast of the rift edge/trough is effectively spread over more pixels. This lowers the length to width ratio of the feature within a given window, and consequently reduces the ability of NeRD to detect it. To assess this effect of resolution on feature contrast, we apply NeRD on 10×10 windows of high-resolution images (30 m pixel resolution), and down-sampled versions of the same images (90 m pixel resolution). We down-sampled the images from 30 m to 90 m pixel resolution using a nearest neighbour approach that ensures that the contrast between every pixel group is enhanced. See an example for these two resolutions in Fig. 3a and c.

For both the window size and pixel resolution tests, NeRD was applied to Sentinel-2 median image composites of DJF 2020–2021 in the Amundsen Sea Embayment study area. The number of detected damage pixels were counted, including all pixels where $\hat{D} > 0$, to allow a pixel-wise comparison between the individual experiments. To this end, the results of the low resolution tests (750 m window size or 90 m pixel resolution) were re-sampled back to the same grid as the high-resolution tests (300 m window size or 30 m pixel resolution).

4.1.2. Sensor sensitivity

In the sensor sensitivity experiments we tested the effects of (i) different spectral bands in optical data and (ii) different data sources (optical versus SAR) on the obtained the damage product. For this purpose, the NeRD method was applied to the red (R; B4), green (G; B3), blue (B; B2), and short-wave Infrared (SWIR; B11) bands of a Sentinel-2 median image composite (DJF 2019–2020) individually. Next, the robustness of the NeRD method to data acquired from different sensors was tested by applying it to both optical Sentinel-2 and Landsat 8 data and Sentinel-1 SAR data, which all were sampled to the same 30 m grid resolution to allow direct comparison. For this sensitivity experiment all images were processed on 10×10 pixel windows (30 m pixel resolution).

4.2. Application of NeRD

We have applied NeRD to the Amundsen Sea Embayment study area on Sentinel-2 median image composites of DJF 2020–2021. The images were processed on 10×10 pixel windows (300 m), based on the outcome of the sensitivity tests. The damage signal $\hat{D}$ was quantified

Table 1
Crevasse signal threshold τ_{crev}, defined as the averaged crevasse signal value, $\overline{\sigma_{crev}}$, for undamaged areas. Values are aggregated for all windows in selected undamaged areas. Values are calculated depending on window size and data source.

Window size		Number of windows	Crevasse signal threshold, τ_{crev}			
			Sentinel		Landsat	
			S1	S2	L7	L8
150 m	5×5 px	8732	0.058	0.046	0.027	0.049
300 m	10×10 px	2251	0.050	0.040	0.032	0.051
700 m	25×25 px	376	0.044	0.039	0.037	0.065
3300 m	110×110 px	27	0.042	0.034	0.027	0.031

following Eq. (5), for which a representative value of $\tau_{crev} = 0.040$ was determined (see next Section 4.2.1).

After validation of the results in the study area we applied NeRD with the same 10×10 px window size to a timeseries of median image composites on the Pine Island Glacier, consisting of two Landsat 8 median composites (DJF 2013–2014 and 2015–2016) and two Sentinel-2 median composites (DJF 2017–2018 and 2019–2020). This was done to analyse the temporal consistency of NeRD in more detail.

4.2.1. Noise removal

The threshold (τ_{crev}) is a representative signal value of typical undamaged, noisy windows that is used to remove noise from the crevasse signal (Eq. (5)). This noise value depends on the variability of pixel intensity values within the processing window. What this means is that it can vary with different window sizes, as this will impact the signal-to-noise ratio of a feature. Moreover, τ_{crev} will vary with the use of a different data source since the amount of noise in the image differs between optical and SAR sources. τ_{crev} was therefore calculated for all window sizes used in this study, which range from 5×5 to 110×110 pixels, in combination with each Sentinel-1/2 and Landsat 7/8 data source. Although not every window size is used in combination with every data source, τ_{crev} is calculated for every combination to demonstrate its variability between data sources.

We selected three areas on the Pine Island (58 km²), Dotson (27 km²) and Getz (36 km²) glaciers that do not show any apparent signs of damage in the Sentinel-2 median composites and then exported images within the same area for every data source. Using these 'undamaged'

areas, the crevasse signal threshold τ_{crev} was calculated as the mean crevasse signal value of all undamaged windows:

$$\tau_{crev} = \overline{\sigma_{crev,undamaged}}. \tag{7}$$

The resulting τ_{crev} values are shown in Table 1 and range from $\sigma \approx 0.03$ to 0.06. Changes of τ_{crev} between different window sizes are small. τ_{crev} changes more significantly from data source to data source: for 10×10 pixels, τ_{crev} ranges from low thresholds 0.032 (Landsat 7) and 0.040 (Sentinel-2) to high thresholds 0.050 (Sentinel-1) and 0.051 (Landsat 8).

4.3. Validation

Validation of NeRD method consisted of two comparisons: (i) a comparison of detected damage pixels to manually labelled ground-truth damage map and (ii) a comparison with the CNN fracture map of Lai et al. (2020).

Firstly, a manually labelled damage map was constructed using QGIS (QGIS Development Team, 2009) on the Sentinel-2 median image composites of DJF 2020–2021 in the Amundsen Sea Embayment area (30 m resolution). QGIS enables an interactive and dynamic view of the image, allowing us to map multiple types of damage features, including: (i) individual linear features, (ii) polygons with densely crevassed fields and (iii) polygons with heavily damaged, disintegrated areas with open rifts and ice mélange. Polygons covering surface crevasse fields or heavily damaged areas are visibly distinctive by the feature size included in the area. The identified linear features can indicate rifts, snow covered rifts, or basal crevasses (McGrath et al., 2012b). The resulting labels are shown in Supplementary Figure 2. We predominantly identify surface crevasse fields on the ice tongue of Pine Island glacier, heavy damage in the shear zones of Pine Island, Crosson and Thwaites glaciers, and large linear features predominantly on Crosson and Getz glaciers. The labelled damage vectors were rasterised onto the 300 m grid of the produced damage maps, to determine True Positive (TP), True Negative (TN), False Positive (FP) and False Negative (FN) detected pixels. With these, the accuracy, precision, recall and f1-score metrics were calculated to assess the performance of NeRD (Stehman, 1997; Taha and Hanbury, 2015):

$$accuracy = \frac{TP + TN}{P + N},$$
$$precision = \frac{TP}{TP + FP},$$
$$recall = \frac{TP}{TP + FN},$$
$$f1 - score = \frac{FP}{N}.$$

Because of a strong imbalance between the number of damaged to undamaged pixels the macro-averaged f1-score was calculated. This is the unweighted mean of the metrics calculated for each label, and gives a relatively high penalty to errors in the minority (damaged pixels) class (Taha and Hanbury, 2015).

Second, NeRD was compared in a two-resolution approach to the CNN fracture map of Lai et al. (2020). The CNN architecture consists of multiple convolution and max-pooling layers that encode and decode the data. The input/output resolution is 125 m, corresponding to the MOA2009 dataset to which the CNN is applied. The receptive field of the CNN, however, spans 3500 m for each pixel (calculated based on Araujo et al. (2019)). We therefore compare results from NeRD to both these scale levels. To this end, we applied NeRD on a Landsat 7 DJF 2008–2009 median image composite which covers the same austral summer as MOA2009 (Haran et al., 2021), at two resolutions: once using 5×5 pixel windows and 110×110 pixel windows (30 m pixel resolution). This corresponds to 150 m and 3300 m window sizes respectively, thus comparing detected damage at similar resolutions as the CNN input/output and receptive field resolution. Additionally, NeRD was applied directly to the 125 m resolution MOA2009 image

itself, with a 10×10 pixel window size (1250 m). The combination of these approaches allows to compare (a) the ability of NeRD and the CNN to resolve damage features and (b) the likeness of the results when applied to the same data.

5. Results

5.1. Sensitivity analysis

5.1.1. Resolution sensitivity

The map and bar-chart in Figs. 4 and 5 show the sensitivity of NeRD to window size and pixel resolution, highlighting that the changes in detected damage pixels in both resolution sensitivity tests are small as both high and low resolution tests detect similar features. Although the detected damage area is somewhat larger in the low resolution tests, Fig. 4 shows that this increase in damage area occurs adjacent to the high-resolution detected damage areas. These pixels therefore do not necessarily represent newly detected damage features, but mostly represent a widened detection of the same features. We therefore make a distinction in the bar-chart in Fig. 5, where damaged pixels are grouped into four classes: (i) pixels that are detected in both pixel- or both window resolution tests (blue bars), (ii) pixels that are detected only by low pixel- or low window resolution test, but are directly adjacent to high resolution detected damage pixels (green bars), (iii) the remaining pixels that are detected only by low resolution test (pink bars), and (iv) pixels that are detected only in the high resolution test (orange bars). As group (i) and (ii) represent the same features, they can be combined for interpretative purposes.

On Pine Island, Thwaites and Crosson ice shelves, approximately 50% of the total damaged pixels are detected by both pixel- or both window resolution tests (blue bars). Adding to that the adjacent detected damage pixels of group ii (green bars), the figure shows that a total of 73%–83% of the detected damage features are represented in both resolution tests on these three ice shelves. On Pine Island, 13.4% (18.9%) damage pixels are detected by only the high pixel (window) resolution tests (orange bars), versus 8.1% (7.7%) pixels by only the low pixel (window) resolution tests (pink bars). In this case a lower pixel (window) resolution decreases the detection of damage features: a net effect of −5.3% (−11.2%). For the other ice shelves, however, the lower resolution tests yields roughly the same or more detected damage features. The latter is especially the case on Getz ice shelf, where 26.2% (19.0%) of the damage pixels are detected only by the low pixel (window) resolution tests, with respect to 10.5% (7.5%) pixels that are only detected by the high resolution tests - a net increase of 15.7% (11.5%). Fig. 4d and h show that this increase in detected damage pixels improves the detection of large rifts. The effect is larger for the low pixel resolution tests (90 m pixel resolution) than for the low resolution window size test (25×25 pixels), indicating that down-sampling the high resolution image with contrast enhancement benefits the detection of these wide linear features.

Overall, the sensitivity tests highlight that NeRD is robust to choice of window size and pixel resolution: the changes in detected damage pixels are small and changes in detected damage patterns minimal. A reduction of pixel/window resolution can increase as well as decrease the detected damage features, but is only beneficial for areas with predominantly (large) linear damage features. With this in mind, and the intention to get a high resolution damage map of multiple types of damage, we therefore continue with the application of NeRD on 30 m pixel resolution images, applied to 10×10 pixel window sizes.

5.1.2. Sensor sensitivity

This experiment considers both sensitivity of NeRD to the choice of spectral bands in optical data, as well as the differences when applied to optical or SAR data.

We show the sensitivity of NeRD to the R, G, B and Short-Wave Infra Red (SWIR) spectral band of Sentinel-2 (spatial mosaic of DJF 2019–2020) in Fig. 6. The figure displays detected damage for each spectral
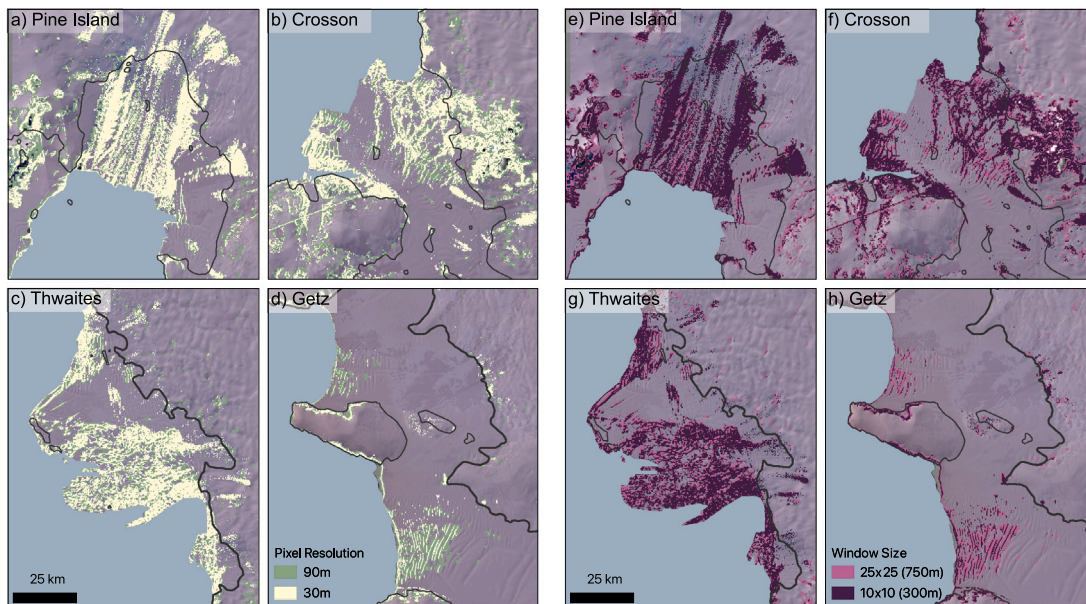
Fig. 4. Figure showing the pixels where damage is detected (classified if $\hat{D} > 0$) for two the resolution sensitivity experiments on the selected ice shelves in the study area: Pine Island (panel a & e), Thwaites (panel b & f), Crosson (panel c & g) and Getz (panel d & h). Panels a–d show detected damage for different pixel resolutions: the native resolution of 30 m per pixel versus a down-sampled resolution of 90 m per pixel. Panels e–h show detected damage for different window sizes: size 10 × 10 pixels (300 m) and 25 × 25 pixels (750 m). The background shows the Sentinel-2 RGB median image composites (DJF 2020–2021) on which the experiments were applied. Grounding lines (dark grey line, Rignot et al. (2016)) and an ocean mask (light blue area, adjusted from Mouginot et al. (2017b)) are added to the plot. (For interpretation of the references to colour in this figure legend, the reader is referred to the web version of this article.)
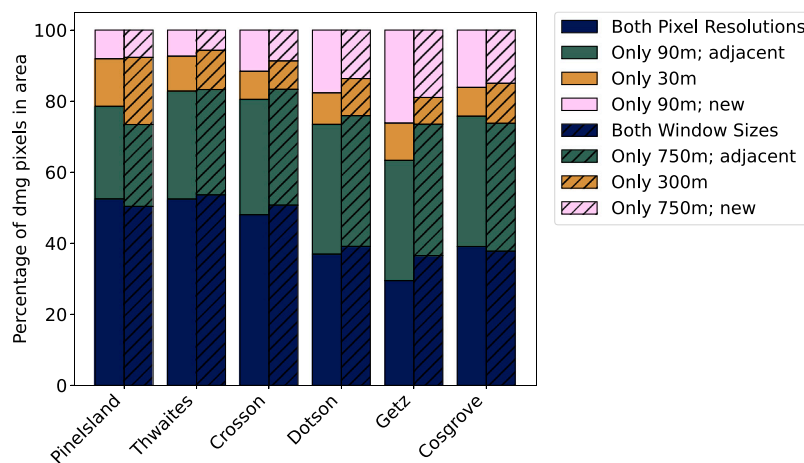

Fig. 5. Bar-chart of detected damage pixels grouped per ice shelf, normalised for the total number of pixels detected by both pixel resolution tests (uniform bars) or both window resolution tests (hashed bars) on that ice shelf. The pixels are grouped by: pixels that are detected in both pixel- or both window resolution test (blue bars), pixels that are detected only by the low resolution test but are directly adjacent to high resolution detected damage pixels (green bars), the remaining pixels that are detected only by low resolution test (pink bars), and pixels that are detected only in the high resolution test (orange bars). (For interpretation of the references to colour in this figure legend, the reader is referred to the web version of this article.)

band individually (Panel a, b, c, e) with the original band data in the top row. Panel (d) shows an RGB plot of the individual bands (top) and cumulative detected damage on the individual R, G, B bands (bottom), such that the colour scheme indicates in which band(s) damage has been detected. The majority of the pixels in panel (d) are coloured white, meaning damage is detected in all bands. This test confirms that differences between R, G and B bands are small, and that the most complete detection will be achieved when using all three bands. This test also shows that the SWIR band is very sensitive to any remaining cloud properties or variability of this band between individual scenes that are used to construct the DJF image. Because of this, we have excluded SWIR as a potentially useful band.

Fig. 7 and Table 2 show the results of the second sensitivity test. For this, NeRD is applied to three different data sources: Sentinel-2, Landsat 8 and Sentinel-1 respectively. Table 2 shows that NeRD detects almost twice as much damage pixels in the Sentinel-1 image than in the Sentinel-2 and Landsat 8 images. Despite this quantitative difference, the map in Fig. 7 clearly shows that the areas with high damage signal values are detected on all data sources. This includes almost the entirety of the western shear zone, the ice front and the damage in the Western tributary. This result indicates the robustness of the method to identify the consistent heavy damage patterns across the different data types.

Most of the pixels that are detected in Sentinel-1 but not in Landsat 8 or Sentinel-2 are pixels with low damage signal values ($\hat{D} < 0.10$); see Fig. 7d. Moreover, these pixels are located mainly on the ice shelf
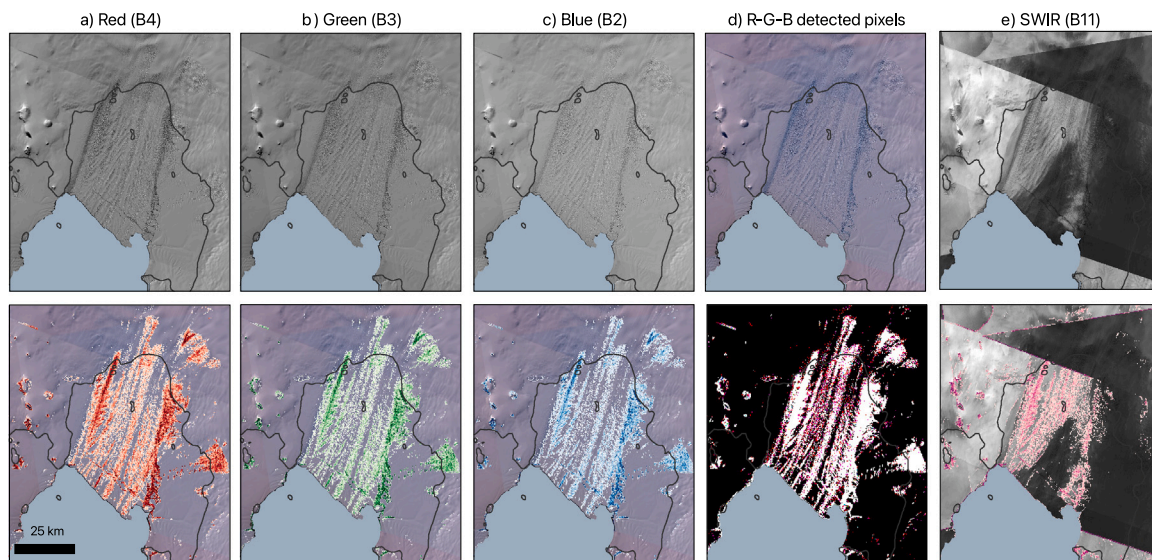
Fig. 6. Figure showing the detected damage using the NeRd method applied to the separate optical bands (a) Red, (b) Green, (c) Blue and (e) Short-Wave Infra-Red of a Sentinel-2 image of the summer 2019–2020 (d, top). Panel (d, bottom) shows an RGB plot of the Red, Green and Blue band together, such that colour scheme indicates in which band(s) damage has been detected. A red colour indicates damage detected only in the red band, and similar for green and blue colours; a purple colour is damage detected in both red and blue bands. White indicates that damage is detected in all three bands. Grounding lines (dark grey line, Rignot et al. (2016)) and an ocean mask (light blue area, adjusted from Mouginot et al. (2017b)) are added to the plots. (For interpretation of the references to colour in this figure legend, the reader is referred to the web version of this article.)
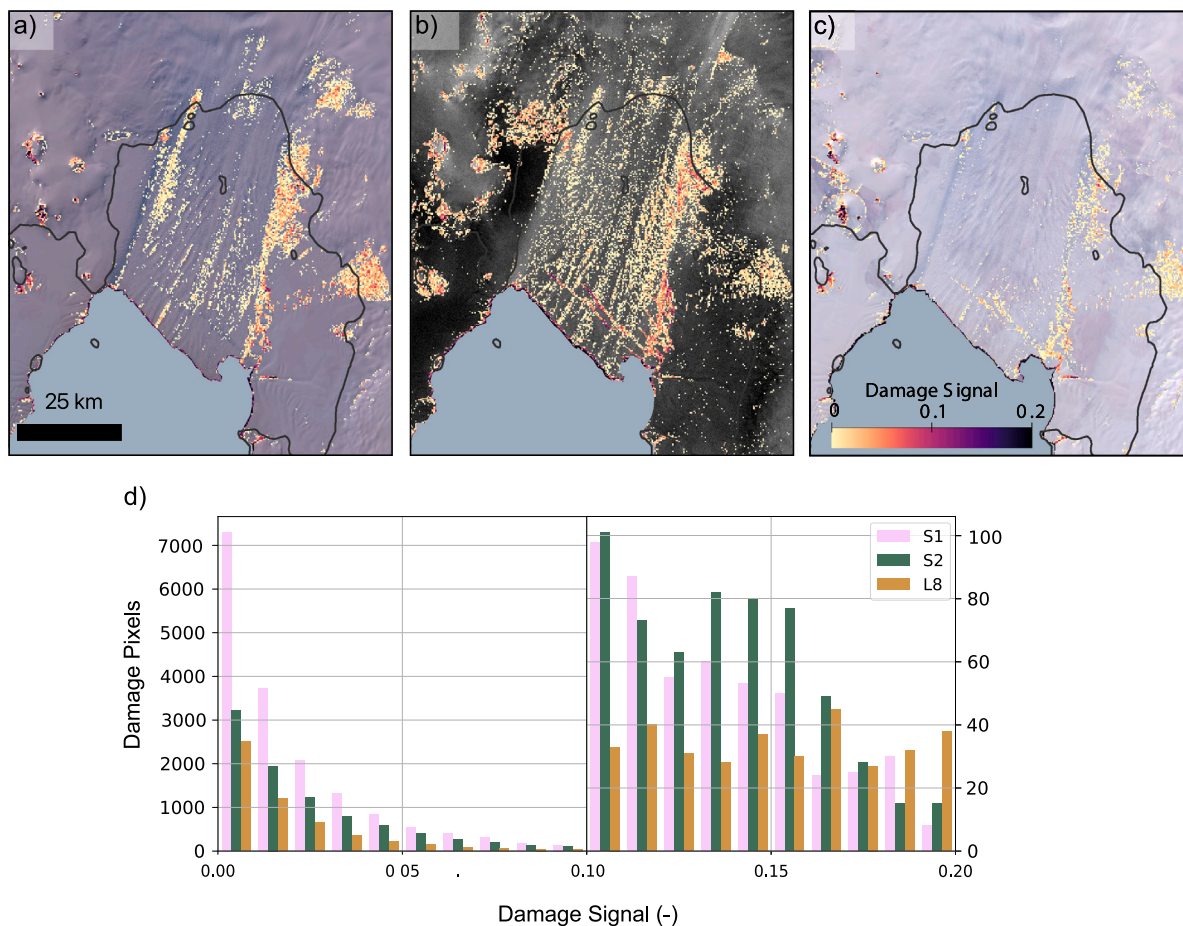
Fig. 7. Damage detected on images of the Pine Island Glacier in December 2019 for (a) Sentinel-2, (b) Sentinel-1 and (c) Landsat 8 image, using window sizes of 10 × 10 pixels (300 m). (d) shows the binned pixel count of detected damage pixels for the range of damage signal values for each source. Sentinel-2 and Landsat 8 images are median composites and Sentinel-1 is a spatial mosaic of DJF 2019–2020. Grounding lines (dark grey line, Rignot et al. (2016)) and an ocean mask (light blue area, adjusted from Mouginot et al. (2017b)) are added to the plot. (For interpretation of the references to colour in this figure legend, the reader is referred to the web version of this article.)
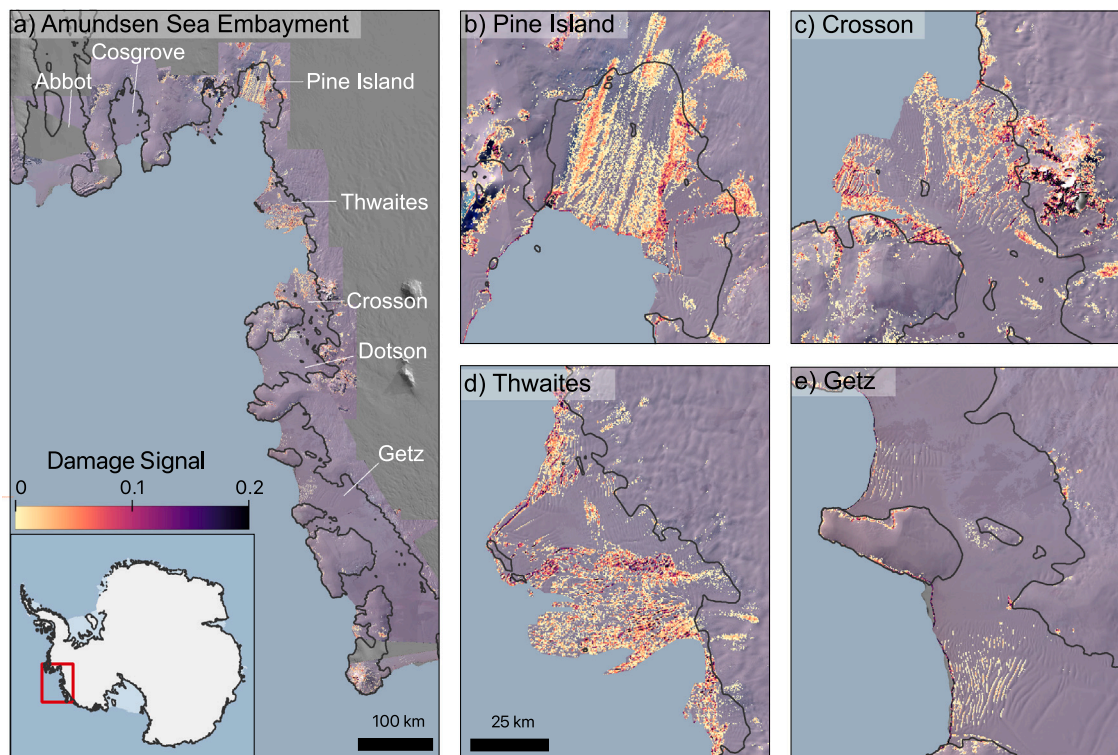
Fig. 8. Detected damage ($\hat{D}$), as result of the NeRD method, applied to ice shelves in the Amundsen Sea Embayment on Sentinel-2 median image composites for DJF 2020–2021, using red (B4), green (B3) and blue (B2) spectral bands. Panel (a) shows the full study area, panel (b–e) show zoom boxes for selected ice shelves. Grounding lines (dark grey line, Rignot et al. (2016)) and an ocean mask (light blue area, adjusted from Mouginot et al. (2017b)) are added to the plot. (For interpretation of the references to colour in this figure legend, the reader is referred to the web version of this article.)

Table 2

Detected damaged pixels counted for the different sensors, Sentinel-2 (S2), Sentinel-1 (S1) and Landsat 8 (L8). The table compares (not) overlapping detected damage pixels between the sensors. Each row compares the percentage of that sensor that overlaps with the other in the columns. The cell that displays the overlap of a sensor with itself (i.e. overlap of Sentinel-2 with Sentinel-2) is printed in italic, which indicates the amount of pixels that is only detected by that sensor and no other.

	Total $\hat{D}$ px	Detected px in combination with sensors..			
		All-sensors (%)	.. with S1 (%)	... with L8 (%)	.. with S2 (%)
Sentinel-2	9442	33.5	25.8	12.7	*28.0*
Landsat 8	5939	53.2	9.8	*16.7*	20.3
Sentinel-1	16 975	18.6	*63.6*	3.4	14.3

tongue, where mostly small scale surface crevasses are found. The difference in detection between SAR and optical data on these small scale features can be attributed to the pre-processing of the data sets. The use of median composites for optical data results in a blurring effect, caused by ice displacement. This blurring also explains why the large open rift near the ice front is only partially detected in the optical images.

Overall the results of the sensor sensitivity indicate the robustness of the method to consistently identify damage patterns across the two data types. Although the amount of detected damage varies, differences arise mostly for low damage values. This result emphasises the complementarity of SAR and optical data for damage detection.

5.2. Damage detection at the amundsen sea embayment

Fig. 8 shows the damage detected as result of the NeRD method across the ice shelves in the Amundsen Sea Embayment. Most damage pixels and the strongest damage signals ($\hat{D}$) are detected on the Pine Island, Crosson and Thwaites ice shelves. The results show moreover

that high damage signals ($\hat{D} > 0.1$) are mostly found in the shear zones of these ice shelves, while lower damage values are detected on the ice tongues. Inspection of the source imagery (Supplementary Figure 1) shows that these areas with high damage signal values consist of heavily damaged ice, containing fully fractured rifts and ice mélange, while the damage area on the ice tongue are mostly surface crevasses (Supplementary Figure 2). NeRD also detects large linear rifts near the ice front of the Getz ice shelf, although these rifts show lower damage signal values: $\hat{D} \approx 0.02$ to 0.03. This lower value of $\hat{D}$ can be explained by lower image contrasts of rifts as a result of snow cover. This lower contrast also explains why the rifts in the upstream area of Getz are not detected by NeRD as the contrast in their cross-section is even lower there.

NeRD also detects the ice front for many of the ice shelves in the Amundsen Sea Embayment. The sharp gradient of the bright calving front and the darker sea in the optical images results in a strong damage signal. Although the calving front is not considered damage in the scope of this study, calving front detection could be considered a useful by-product of the NeRD method.

Interpretation of the NeRD damage on the grounded ice is more complicated than on the floating ice shelf. For example, nunataks upstream of Crosson ice shelf create shadows and contrast edges over the surrounding ice that are falsely detected as damage, as well as the coastline. Further post-processing can remove this by masking all the grounded ice or adding an ice height constraint to the data. We have refrained from doing so now, to fully illustrate NeRD capacities.

5.2.1. Damage orientation

The orientation of the damage features ($\alpha_{\hat{D}}$) are displayed as a quiverplot in Fig. 9, scaled in size to their respective damage signal value. For Pine Island, Thwaites, Crosson and Getz ice shelves a small part of the ice shelf is selected to comprehensibly visualise the detected damage orientations.
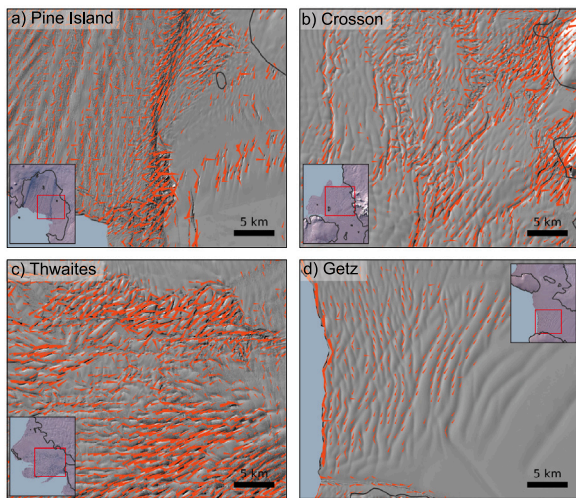
Fig. 9. Detected damage orientation ($\alpha_{\hat{D}}$) for selected areas on (a) Pine Island, (b) Crosson, (c) Thwaites and (d) Getz ice shelves, as result of NeRD applied on Sentinel-2 median image composites for DJF 2020–2021, shown in grey-scale as background. The quivers are rotated with $\alpha_{\hat{D}}$ degree angles and scaled relatively to the damage signal value $\hat{D}$. For visual clarity the number of plotted quivers is reduced to one median value for every 3×3 pixel group.

Firstly, Fig. 9 shows a good alignment of detected damage orientations to the visible edges of damage features. This is clear on Crosson and Getz ice shelf, where large rifts are tracked well, including a consistent alignment to the calving front (detected as damage feature) on Getz ice shelf and the consistent detected orientation of the two edges of open rifts on Crosson. In the shear zone of Pine Island, Crosson and Thwaites ice shelves the damage orientations are more chaotic, especially in the presence of ice rubble. Thwaites shows a relatively aligned damage field due to the block-wise structure of ice bergs in combination with the sun incidence angle that enhances the shadows of ice edges in one direction.

5.3. Validation

5.3.1. Validation to manual labels

The validation of detected NeRD damage with manually labelled damage is shown in Fig. 10, displaying true negatives (TN), false negatives (FN), false positives (FP) and true positives (TP). The corresponding confusion matrices are included in Supplementary Figure 3.

Firstly we note that the validation shows frequent detection of false positive damage pixels on grounded ice, which is especially prevalent upstream of Pine Island and Crosson ice shelves. This is the result of the earlier mentioned difficulties with terrain shadows. These false positive pixels over grounded ice restrict the obtained macro averaged precision in the Amundsen Sea Embayment study area to 0.69. For further validation metric calculations, all grounded ice was removed using the grounding line from Rignot et al. (2016). The grounded ice pixels are still visualised in Fig. 10 to give a full representation of the validation. Removing the damage detection on grounded ice increases the macro averaged precision in the study area to 0.81.

The validation results show a good overall performance of the NeRD method, with an accuracy of 0.95 across all ice shelves in the study area and a macro averaged f1-score of 0.80. The macro averaged f1-score on Pine Island, Crosson, Thwaites and Getz ice shelves are 0.79, 0.79, 0.77 and 0.69, respectively. For Pine Island, Crosson and Thwaites the macro averaged precision and recall are of similar value, all between 0.77 and 0.80. The relatively low f1-score for Getz ice shelf is the result of low recall (0.64) rather than precision (0.81).
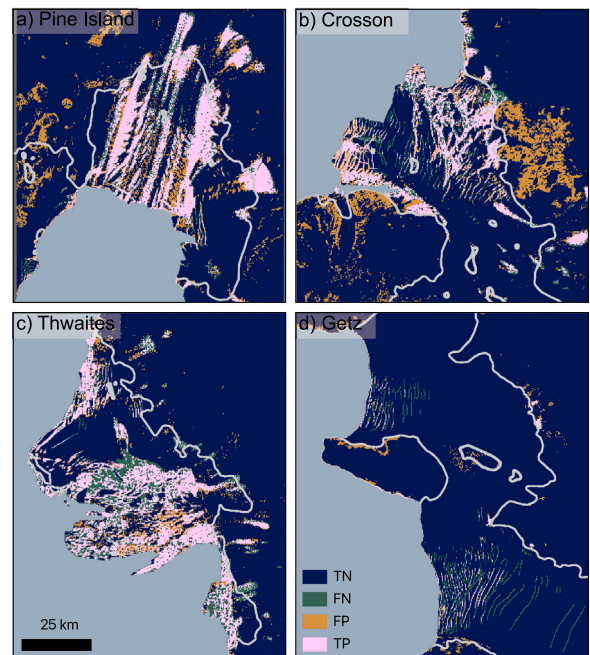

Fig. 10. Performance of detected damage using the NeRD method, validated against manually labelled damage features. Pixels are classified as True Positive (TP, pink), False Positive (FP, orange), False Negative (FN, green) and True Negative (TN, blue). Grounding lines (light grey line, Rignot et al. (2016)) and an ocean mask (light blue area, adjusted from Mouginot et al. (2017b)) are added to the plot. (For interpretation of the references to colour in this figure legend, the reader is referred to the web version of this article.)

These good performances are reflected in Fig. 10, which shows a good representation of true positive detected damage pixels across the ice shelf tongues and in the shear zones. The limited number of false positive pixels (excluding grounded ice) explains the high precision, whereas the relatively sparse number of false negative pixels explains the high recall for most ice shelves. Only on Getz ice shelf the ratio of false negative pixels is relatively high, as a result of NeRD's difficulty to detect some of the wide upstream rifts. Moreover, the majority of false positive pixels on the ice shelves are located directly adjacent to true positive pixels. In many cases, this suggests a wider damage detection than that is labelled, rather than the detection of non-existing damage features.

In summary, the validation shows an overall good performance of the NeRD method to detect damage. The fact that the precision is consistent for the damage detected at all ice shelves in the Amundsen Sea Embayment indicates a robust damage detection method.

5.3.2. Comparison to fracture map

The comparison between the NeRD detected damage map and the fracture map of Lai et al. (2020) in Fig. 11 shows different damage patterns for both methods on all four ice shelves. NeRD has been applied to Landsat 7 images on 150 m (5×5 pixels) and 3300 m (110×110 pixels) windows. For both, NeRD detects the same major damage areas, with some new areas showing up in the 3300 m results and some small scale features disappearing (e.g. on Thwaites ice tongue). The nuances due to resolution have been discussed in Section 5.1.1, whereas this Section will focus on the difference between the damage detected by NeRD and Lai et al. (2020). Seeing the similarities between the 150 m and 3300 m damage maps, we continue the comparison to the fracture map with a focus on the 150 m resolution damage map.

Generally, the CNN fracture map of Lai et al. (2020) displays more linear features. This includes larger, more gradual, rifts and folds (Fig. 11). This CNN method works well on the Getz ice shelf, where
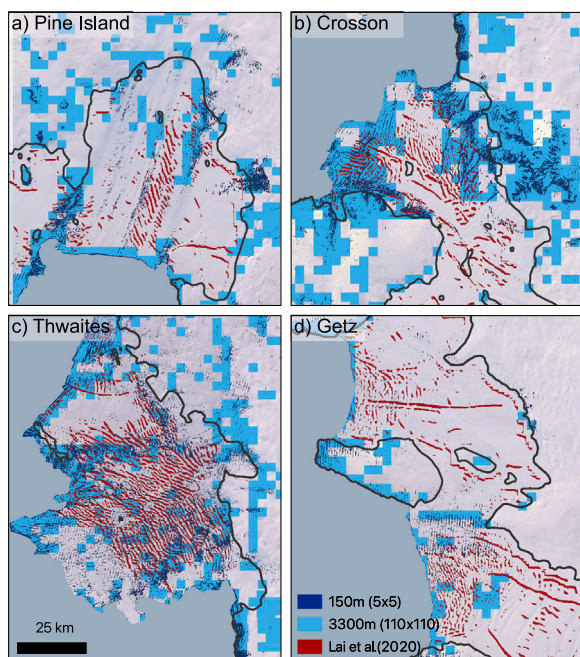
Fig. 11. Detected damage (classified if $\hat{D} > 0$) on the Landsat 7 median image composite (background) for summer 2008–2009 on the selected ice shelves in the study area: (a) Pine Island, (b) Thwaites, (c) Crosson and (d) Getz ice shelves. Blue values indicate the detected damage as result from the NeRD method, applied to 110×110 pixel windows (3300 m, light blue, bottom layer) and 5×5 pixel windows (150 m, dark blue, top layer). Red values (middle layer) represent the detected fractures by Lai et al. (2020) using a machine learning approach, applied to the MODIS Mosaic of Antarctica 2008–2009 (MOA2009) on 125 m pixel resolution but based on a 3500 m receptive field. Grounding lines (dark grey line, Rignot et al. (2016)) and an ocean mask (light blue area, Mouginot et al. (2017b)) are added to the plot. (For interpretation of the references to colour in this figure legend, the reader is referred to the web version of this article.)

the CNN method detects most of the large rifts that are missed by the NeRD method. However, a down-side of the CNN's focus on large linear shapes is that the fracture map also includes flow lines that are morphological similar to these rifts (Ely and Clark, 2016). The benefit of NeRD is that, despite missing some of the large rifts, it correctly omits detection of flow lines.

We see a strong difference in performance between the CNN and NeRD method on the Pine Island and Crosson ice shelves. The CNN fracture map detects crevasse field areas on the ice tongues as a single fracture. These areas stand out with respect to the rest of the ice shelf tongue due to snow cover patterns. More importantly, the CNN method completely overlooks the erratically organised damage in the shear zones on both these ice shelves.

Also on Thwaites ice shelf NeRD detects high damage areas in the shear zone between the Eastern ice shelf and main tongue which are missed in the CNN fracture map. The CNN method, moreover, detects more linear patterns on the main ice tongue. This can be explained by the resolution of the used dataset: on the MOA2009 image with 125 m pixel resolution, the ice fractures are indeed linearly oriented. On the higher resolution Landsat 7 image (30 m) the ice tongue displays a more block-like organisation of the ice.

To conclude: on the one hand, the NeRD method might overlook some wide and gradual rifts, as is characteristic on the Getz ice shelf and correctly detected by the CNN. On the other hand, the CNN fracture map of Lai et al. (2020) consistently overlooks heavy damage patterns that have an irregular shape, and also wrongly detect flow lines as fractures.

5.4. Damage evolution

We analyse the evolution of damage over time by applying NeRD to satellite imagery of multiple years. Fig. 12 shows an example time series of detected damage on Landsat 8 and Sentinel-2 median image composites of the Pine Island ice shelf during the austral summers of 2013–2014, 2015–2016, 2017–2018 and 2019–2020.

This time series show that the damage in the shear zones increased from 2013 to 2019. The ice tongue shows a more intra-annual variability: damage increases from 2013 to 2018 but then decreases in 2019 back to a similar pattern as 2015. This larger variability for the smaller surface crevasses on the ice tongue can be explained by two aspects. First, varying snow cover conditions can hide or reveal crevasses in the optical images of Landsat or Sentinel. On top of that, the number of images that are used for the median composite varies per season, depending on the number of images that pass the cloud filter, enhancing (many images) or reducing (few images) the blurring effect of the median image composite. This shows that a seasonal or annual variability related to surface crevasses can be imposed on the damage map.

The zoom-boxes in Fig. 12 show initiation and evolution of damage in the western shear-zone of the Pine Island ice shelf. Large rifts first appeared in DJF 2013–2014 (panel a) and have opened and grown by DJF 2015–2016 (panel b). NeRD successfully tracks the rotation and opening of the rifts, aligning the detected damage orientation to the rift's edge. By DJF 2019–2020 (panel d), the individual rifts are no longer distinguishable and the area has become heavily damaged with little intact ice remaining. Hence, a more chaotic pattern of damage orientations is detected. All the while, the orientations of the crevasses on the ice tongue are quite consistently oriented throughout the years, and show a relatively aligned field of orientation. These crevasses are likely related to the vertical flexing of the ice shelf in response to the formation of basal melt channels, rather than changes in the local strain field (Vaughan et al., 2012), which can explain their consistent alignment.

The consistent tracking from developing rifts to disintegrated areas, both in terms of damage signal and orientation, indicates the qualitative performance of the method to detect damage.

6. Discussion

The different NeRD experiments have shown that the proposed NeRD method detects damage signal values primarily based on feature contrast rather than feature intensity. This removes false signals and dependencies on processing window size, both of which are prevalent in the classical Radon Transform. NeRD enables an automated application on different images and for different regions. This is in contrast to other damage detection methods, such as a CNN method that needs re-training for every data set, or manual mapping that is labour intensive and depends on expert judgement.

Sensitivity tests show that the detected damage product can change between −11 to +15% as a result of reducing the window or pixel resolution. The increase or decrease of detected damage pixels depends mainly on the type of damage features represented in the area. For heavily damaged ice shelves like Pine Island, Thwaites and Crosson, high resolution yields more detected damage. NeRD is most sensitive to a reduction of resolution in areas with wide features, as is seen on Getz ice shelf. In these areas, detection would improve by a reduced pixel/window resolution. As Cosgrove and Dotson ice shelves show similar sensitivity to window/pixel resolution as Getz ice shelf, we expect other lightly damaged ice shelves across the Antarctic to behave similarly. That aside, the sensitivity tests show a very robust and consistent detection of damage patterns.

With the NeRD method we are able to generate damage maps that can be analysed across space and time, because the quantified damage value is consistent for different spatial or temporal domains.
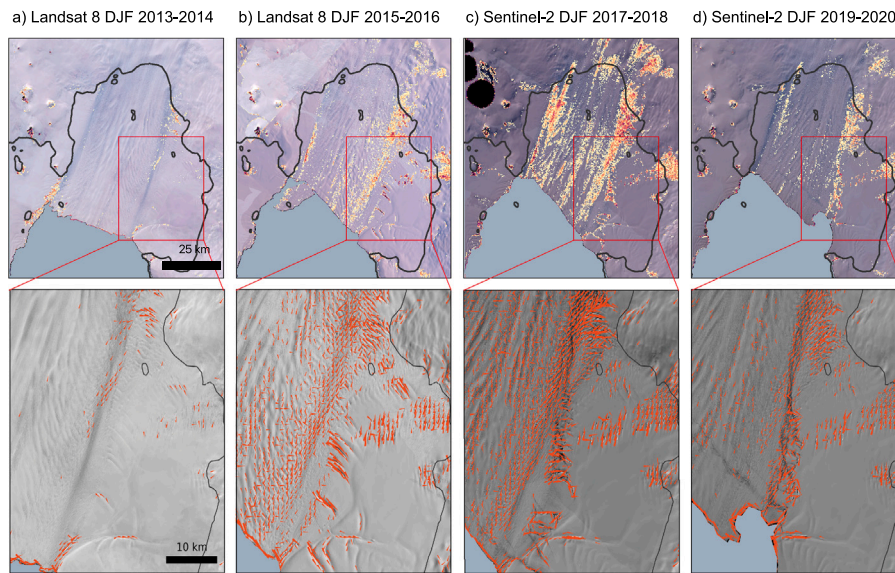
Fig. 12. A timeseries of detected damage signal (top row) and damage orientation (bottom row) for damage detected on Landsat 8 and Sentinel-2 median image composites of the Pine Island Glacier during the summers (DJF) of (a) 2013–2014, (b) 2015–2016, (c) 2017–2018 and (d) 2019–2020. The zoom-boxes show the damage orientation in the western shear-zone close to the ice front, with the length of the quiver scaled to the strength of the damage signal. Grounding lines (dark grey line, Rignot et al. (2016)) and an ocean mask (light blue area, adjusted from Mouginot et al. (2017b)) are added to the plot. (For interpretation of the references to colour in this figure legend, the reader is referred to the web version of this article.)

This improves upon the previous crevasse map from Gong et al. (2018). Moreover, results consistently quantify damage patterns for all three tested data sources, paving the way for synergistic multi-source damage detection that overcomes remaining limitations from individual sources. The differences between damage detected from either optical or SAR data occur mainly for surface crevasses. Differences are caused primarily by the image pre-processing approach and by the image quality which is affected by clouds, shadows or illumination conditions, rather than by the NeRD method itself. The blurring effect that occurs in optical data due to compositing is a source for underestimated damage detection. Alternative to median composites one could construct spatial mosaics for optical data as well, which yields similar details of damage detection as shown on SAR data. Optical spatial mosaics, however, are much more susceptible to the mentioned image quality aspects than median composites (included in Supplementary Figure 5). This then would require more careful pre-processing, which did not fit the objective to develop an automated approach that can be applied out-of-the box to any data source.

With NeRD we are able to detect multiple types and scales of damage features. This is an improvement with respect to existing fracture maps. The fracture map of Lai et al. (2020) detects large-scale linear-like fractures on coarse data resolution, and the crevasse map of Bhardwaj et al. (2016) detects crevasses in a densely crevassed field on high-resolution data. The NeRD method is able to detect both densely crevassed fields and large scale rifts, and also includes the heavily damaged areas in the shear-zones. NeRD is a first-of-its kind method that detects continuous rather than binary damage features. It is this characteristic that allows NeRD to include the multiple types of damage features without losing comprehensible interpretation. Moreover, as high values of the detected damage parameter $\hat{D}$ seem to correlate to large (deep) damage features and low values to small (shallow) features, $\hat{D}$ could potentially be linked to the scalar damage factor used in CDM modelling (Borstad et al., 2012, 2013, 2016; Sun et al., 2017) or to vertical crevasse information obtained from laser altimetry studies (Li et al., 2021; Wang et al., 2021). NeRD, however, is less suited to detect wide features with gradual slopes, especially compared to the CNN fracture map of Lai et al. (2020). This detection can be improved by down-sampling the image to enhance edge contrasts, but this is at the cost of spatial resolution of the final product. Furthermore, NeRD

does not perform well in areas with changing terrain features, such as rock outcrops or hill shade. On ice shelves this is mostly a trivial issue, but future studies should take care to mask these features from the image.

The detection of damage orientation in addition to the damage signal adds to the potential uses of NeRD in future research. The robust tracking of rotating rifts can help improve our understanding of damage evolution. Furthermore, the detected damage orientation can be compared to the orientation of principal strain, using velocity data that is a close temporal match to the satellite imagery used for damage detection, which can provide insight in crevasse opening mode and can potentially be of help to initialise anisotropic creep damage models (Murakami et al., 1988; Pralong A., 2006; Huth et al., 2021).

Lastly, an interesting by-product of NeRD is that it detects the ice front quite definitely. This has potential to help improve modelling of calving fronts (Enderlin and Bartholomaus, 2020).

In summary, the NeRD method is robust and applicable for large scale assessments. The method is mainly limited by the quality of the input data. Therefore it is suggested that future studies focus on a robust pre-processing approach that consistently retrieves high quality data, which would combine well to the generalised application of the NeRD method. With such robust pre-processing the NeRD method can be applied to large spatiotemporal domains to allow Antarctic wide assessments, but also an application to year-round SAR data to analyse damage changes on a high temporal resolution.

7. Conclusion

In this manuscript we have shown that the proposed NeRD method allows to robustly detects damage across spatial and temporal domains. The method can be applied directly to different image sources, requiring no additional pre- or post-processing. This generalised application to multi-source imagery is a great advantage over previous fracture detection algorithms. With these characteristics the method is suitable for large scale damage assessments.

The ability of NeRD to detect continuous damage signal values allows detection of multiple damage feature scales. Furthermore, it enables the monitoring of damage development over time. We identified spatially varying damage patterns on the ice shelves in the Amundsen

Sea Embayment, with most damage occurring on Pine Island, Thwaites and Crosson ice shelves. These ice shelves display heavy damage in their shear zones, indicating structural weakening of the ice. The consistent detection of damage orientation by NeRD provides insight in crevasse evolution. We analysed damage growth on the Pine Island ice shelf, showing the initiation, advection and rotation of large crevasses that eventually develop into a disintegrated area.

With the NeRD method large scale damage assessments can be made. This in turn can help evaluate ice sheet models to their modelled damage pattern or possibly even calving front representation, or it can help initialise damage models. Large scale damage maps can also be used to train or evaluate machine learning approaches, or be combined with vertical properties of fractures from laser altimetry studies. Finally, temporal damage maps can potentially be used as an early-warning indication for ice shelves that are transitioning from an intact to a damaged state. In all cases, NeRD can be used as a tool to produce important insights regarding crevasse formation and ice shelf vulnerability.

CRediT authorship contribution statement

Maaike Izeboud: Developed and applied the method, Including preprocessing and postprocessing the data, Writing – original draft. **Stef Lhermitte:** Development of the method and processing of the data, Writing – original draft.

Declaration of competing interest

The authors declare that they have no known competing financial interests or personal relationships that could have appeared to influence the work reported in this paper.

Data availability

The code of the developed NeRD method is available on github, https://github.com/mizeboud/NormalisedRadonTransform. The satellite imagery data used in this study is open-source available. All Sentinel and Landsat images have been acquired and pre-processed in the Google Earth Engine, for which the code is available here: https://code.earthengine.google.com/63b4cf06dffc7c6b5695dbd256e844fd. The MODIS MOA2009 mosaic is available at the National Snow & Ice Data Center (NSIDC): https://nsidc.org/data/nsidc-0593/. The grounding line and ocean mask used in the figures were obtained through the Quantarctica3 dataset for QGIS (Matsuoka et al., 2018). The scientific colour maps batlow and roma (Crameri, 2018) were used in this study to prevent visual distortion of the data and exclusion of readers with colour vision deficiencies.

Funding

This publication is part of the project 'Remote sensing of damage feedbacks and ice shelf instability in Antarctica', with project number ALWGO.2018.043 of the research programme 'User Support Programme Space Research 2018' which is financed by the Dutch Research Council (NWO).

Appendix A. Supplementary data

Supplementary material related to this article can be found online at https://doi.org/10.1016/j.rse.2022.113359.

References

Albrecht, T., Levermann, A., 2012. Fracture field for large-scale ice dynamics. J. Glaciol. 58, 165–176. http://dx.doi.org/10.3189/2012JoG11J191.

Altena, B., 2018. Observing Change in Glacier Flow by Using Optical Satellites (doctoral dissertation). University of Oslo, URL: https://www.duo.uio.no/bitstream/10852/61747/1/Phd_Altena-2018.pdf.

Araujo, A., Norris, W., Sim, J., 2019. Computing receptive fields of convolutional neural networks. Distill 4, http://dx.doi.org/10.23915/distill.00021.

Arndt, J.E., Larter, R.D., Friedl, P., Gohl, K., Höppner, K., 2018. Bathymetric controls on calving processes at pine island glacier. Cryosphere 12, 2039–2050. http://dx.doi.org/10.5194/tc-12-2039-2018, URL: https://tc.copernicus.org/articles/12/2039/2018/.

Benn, D.I., Åström, J.A., 2018. Calving glaciers and ice shelves. Adv. Phys. 3, 1513819. http://dx.doi.org/10.1080/23746149.2018.1513819, URL: https://www.tandfonline.com/action/journalInformation?journalCode=tapx20.

Bhardwaj, A., Sam, L., Singh, S., Kumar, R., 2016. Automated detection and temporal monitoring of crevasses using remote sensing and their implications for glacier dynamics. Ann. Glaciol. 57, 81–91. http://dx.doi.org/10.3189/2016AoG71A496, URL: https://landsat.usgs.gov/Landsat8_.

Borstad, C.P., Khazendar, A., Larour, E., Morlighem, M., Rignot, E., Schodlok, M.P., Seroussi, H., 2012. A damage mechanics assessment of the larsen b ice shelf prior to collapse: Toward a physically-based calving law. Geophys. Res. Lett. 39, http://dx.doi.org/10.1029/2012GL053317.

Borstad, C., Khazendar, A., Larour, E., Rignot, E., Scheuchl, B., Morlighem, M., 2016. A constitutive framework for predicting weakening and reduced buttressing of ice shelves based on observations of the progressive deterioration of the remnant larsen B Ice Shelf. J 43, http://dx.doi.org/10.1002/2015GL067365.

Borstad, C.P., Rignot, E., Mouginot, J., Schodlok, M.P., 2013. Creep deformation and buttressing capacity of damaged ice shelves: theory and application to larsen C ice shelf. Cryosphere 7, 1931–1947. http://dx.doi.org/10.5194/tc-7-1931-2013, URL: https://www.the-cryosphere.net/7/1931/2013/.

Chuter, S.J., Martín-Español, A., Wouters, B., Bamber, J.L., 2017. Mass balance reassessment of glaciers draining into the Abbot and Getz Ice Shelves of West Antarctica. Geophys. Res. Lett. http://dx.doi.org/10.1002/2017GL073087.

Colgan, W., Rajaram, H., Abdalati, W., McCutchan, C., Mottram, R., Moussavi, M.S., Grigsby, S., 2016. Glacier crevasses: Observations, models, and mass balance implications. Rev. Geophys. 54, 119–161. http://dx.doi.org/10.1002/2015RG000504, URL: https://agupubs.onlinelibrary.wiley.com/doi/full/10.1002/2015RG000504.

Colgan, W., Steffen, K., McLamb, W.S., Abdalati, W., Rajaram, H., Motyka, R., Phillips, T., Anderson, R., 2011. An increase in crevasse extent, West Greenland: Hydrologic implications. Geophys. Res. Lett. 38, http://dx.doi.org/10.1029/2011GL048491.

Crameri, F., 2018. Scientific colour maps. http://dx.doi.org/10.5281/zenodo.1243862.

Ely, J.C., Clark, C.D., 2016. Flow-stripes and foliations of the antarctic ice sheet. J. Maps 12, 249–259. http://dx.doi.org/10.1080/17445647.2015.1010617.

Enderlin, E.M., Bartholomaus, T.C., 2020. Sharp contrasts in observed and modeled crevasse patterns at Greenland's marine terminating glaciers. Cryosphere 14, 4121–4133. http://dx.doi.org/10.5194/tc-14-4121-2020, URL: https://tc.copernicus.org/articles/14/4121/2020/.

Fox-Kemper, B., Hewitt, H.T., Xiao, C., Aalgeirsdóttir, G., Drijfhout, S.S., Edwards, T.L., Golledge, N.R., Hemer, M., Kopp, R.E., Krinner, G., Mix, A., Notz, D., Nowiciki, S., Nurhati, I.S., Ruiz, J., Sallée, J.-B., Slangen, A.B.A., Yu, Y., 2021. Ocean, cryosphere and sea level change. In: Climate Change 2021: The Physical Science Basis. Contribution of Working Group I To the Sixth Assessment Report of the Intergovernmental Panel on Climate ChangeScience Basis. Contribution of Working Group I To the Sixth Assessment Report of the Intergover, pp. 1–257.

Gardner, A.S., Fahnestock, M.A., Scambos, T.A., 2019. MEaSUREs ITS_LIVE landsat image-pair Glacier and ice sheet surface velocities: Version 1. http://dx.doi.org/10.5067/IMR9D3PEI28U, Accessed Dec–2020.

Glasser, N., Scambos, T., 2008. A structural glaciological analysis of the 2002 larsen b ice-shelf collapse. J. Glaciol. 54, 3–16. http://dx.doi.org/10.3189/002214308784409017, URL: https://www.cambridge.org/core/product/identifier/S0022143000209805/type/journal_article.

Gong, Y., Zwinger, T., Åström, J., Altena, B., Schellenberger, T., Gladstone, R., Moore, J.C., 2018. Simulating the roles of crevasse routing of surface water and basal friction on the surge evolution of basin 3, Austfonna ice cap. Cryosphere 12, 1563–1577. http://dx.doi.org/10.5194/tc-12-1563-2018.

Gorelick, N., Hancher, M., Dixon, M., Ilyushchenko, S., Thau, D., Moore, R., 2017. Google earth engine: Planetary-scale geospatial analysis for everyone. Remote Sens. Environ. http://dx.doi.org/10.1016/j.rse.2017.06.031.

Haran, T., Bohlander, J., Scambos, T., Painter, T., Fahnestock, M., 2021. MODIS Mosaic of Antarctica 2008–2009 (MOA2009) Image Map, Version 2. NSIDC: National Snow and Ice Data Center, Boulder, Colorado USA, p. hp1. http://dx.doi.org/10.7265/N5KP8037, URL: https://nsidc.org/data/NSIDC-0593/versions/2. Date accessed: 2021-10-30.

Herzfeld, U.C., Trantow, T., Lawson, M., Hans, J., Medley, G., 2021. Surface heights and crevasse morphologies of surging and fast-moving glaciers from icesat-2 laser altimeter data - application of the density-dimension algorithm (DDA-ice) and evaluation using airborne altimeter and planet SkySat data. Sci. Remote Sens. 3, 100013. http://dx.doi.org/10.1016/J.SRS.2020.100013.

Huth, A., Duddu, R., Smith, B., 2021. A generalized interpolation material point method for shallow ice shelves. 2: Anisotropic nonlocal damage mechanics and rift propagation. J. Adv. Modelling Earth Syst. 13, http://dx.doi.org/10.1029/2020MS002292, URL: https://onlinelibrary.wiley.com/doi/full/10.1029/2020MS002292.

Kaluzienski, L., Koons, P., Enderlin, E., Hamilton, G., Courville, Z., Arcone, S., 2019. Crevasse initiation and history within the McMurdo shear zone, Antarctica. J. Glaciol. 65, 989–999. http://dx.doi.org/10.1017/jog.2019.65.

Lai, C.Y., Kingslake, J., Wearing, M.G., Chen, P.H.C., Gentine, P., Li, H., Spergel, J.J., van Wessem, J.M., 2020. Vulnerability of Antarctica's ice shelves to meltwater-driven fracture. Nature 584, 574–578. http://dx.doi.org/10.1038/s41586-020-2627-8.

Lhermitte, S., Sun, S., Shuman, C., Wouters, B., Pattyn, F., Wuite, J., Berthier, E., Nagler, T., 2020. Damage accelerates ice shelf instability and mass loss in Amundsen Sea embayment. Proc. Natl. Acad. Sci. 201912890. http://dx.doi.org/10.1073/pnas.1912890117.

Li, G., Guo, J., Pei, L., Zhang, S., Tang, X., Yao, J., 2021. Extraction and analysis of the three-dimensional features of crevasses in the amery ice shelf based on ICESat-2 ATL06 data. IEEE J. Sel. Top. Appl. Earth Observ. Remote Sens. 14, 5796–5806. http://dx.doi.org/10.1109/JSTARS.2021.3085302.

Lilien, D.A., Joughin, I., Smith, B., Shean, D.E., 2018. Changes in flow of crosson and dotson ice shelves, West Antarctica, in response to elevated melt. Cryosphere 12, 1415–1431. http://dx.doi.org/10.5194/tc-12-1415-2018, URL: https://tc.copernicus.org/articles/12/1415/2018/.

Luckman, A., Jansen, D., Kulessa, B., King, E.C., Sammonds, P., Benn, D.I., 2012. Basal crevasses in Larsen C ice shelf and implications for their global abundance. Cryosphere 6, 113–123. http://dx.doi.org/10.5194/tc-6-113-2012.

Matsuoka, K., Skoglund, A., Roth, G., de Pomereu, J., Griffiths, H., Headland, R., Herried, B., Katsumata, K., Brocq, A.L., Licht, K., Morgan, F., Neff, P., Ritz, C., Scheinert, M., Tamura, T., de Putte, A.V., van den Broeke, M., von Deschwanden, A., Deschamps-Berger, C., Liefferinge, B.V., Tronstad, S., Melvæ, Y., 2018. Quantarctica [Dataset]. Norwegian Polar Institute, URL: https://doi.org/10.21334/npolar.2018.8516e961.

McGrath, D., Steffen, K., Rajaram, H., Scambos, T., Abdalati, W., Rignot, E., 2012a. Basal crevasses on the Larsen C ice shelf, Antarctica: Implications for meltwater ponding and hydrofracture. Geophys. Res. Lett. 39, n/a–n/a. http://dx.doi.org/10.1029/2012GL052413, URL: http://doi.wiley.com/10.1029/2012GL052413.

McGrath, D., Steffen, K., Scambos, T., Rajaram, H., Casassa, G., Lagos, J.L.R., 2012b. Basal crevasses and associated surface crevassing on the larsen c ice shelf, antarctica, and their role in ice-shelf instability. Ann. Glaciol. 53, 10–18. http://dx.doi.org/10.3189/2012AoG60A005.

Meredith, M., Sommerkorn, M., Cassotta, S., Derksen, C., Ekaykin, A., Hollowed, A., Kofinas, G., Mackintosh, A., Melbourne-Thomas, J., Muelbert, M., Ottersen, G., Pritchard, H.D., Schuur, E., 2019. Polar regions. In: IPCC Special Report on the Ocean and Cryosphere in A Changing Climate. pp. 203–320, URL: https://www.ipcc.ch/srocc/.

Miles, B.W.J., Stokes, C.R., Jenkins, A., Jordan, J.R., Jamieson, S.S.R., Gudmundsson, G.H., 2021. Intermittent structural weakening and acceleration of the thwaites glacier tongue between 2000 and 2018. J. Glaciol. 66, 485–495. http://dx.doi.org/10.1017/jog.2020.20.

Mouginot, J., Rignot, E., Scheuchl, B., Millan, R., 2017a. Comprehensive annual ice sheet velocity mapping using landsat-8, sentinel-1, and radarsat-2 data. Remote Sens. 9. http://dx.doi.org/10.3390/rs9040364, URL: http://www.mdpi.com/journal/remotesensing.

Mouginot, J., Scheuchl, B., Rignot, E., 2017b. Measures Antarctic Boundaries for Ipy 2007-2009 from Satellite Radar, Version 2. NASA National Snow and Ice Data Center Distributed Active Archive Center, URL: https://nsidc.org/data/nsidc-0709/versions/2.

Murakami, S., Kawai, M., Rong, H., 1988. Finite element analysis of creep crack growth by a local approach. Int. J. Mech. Sci. 30, 491–502. http://dx.doi.org/10.1016/0020-7403(88)90003-3.

Oppenheim, A.V., Willsky, A.S., 1996. Signal & Systems, second ed. Prentice Hall Signal Processing Series, URL: https://www.academia.edu/37486178/Signals_and_Systems_2nd_Edition_by_Oppenheim_.

Öznergiz, E., Kiyak, Y.E., Kamasak, M.E., Yildirim, I., 2014. Automated nanofiber diameter measurement in SEM images using a robust image analysis method. J. Nanomater. 2014, http://dx.doi.org/10.1155/2014/738490.

Pattyn, F., Morlighem, M., 2020. The uncertain future of the antarctic ice sheet. Science 367, 1331–1335. http://dx.doi.org/10.1126/science.aaz5487, URL: http://science.sciencemag.org/.

Pralong A., F.M., 2006. Anisotropic damage mechanics for viscoelastic ice. Continuum Mech. Thermodyn. 17, 387–408. http://dx.doi.org/10.1007/s00161-005-0002-5.

QGIS Development Team, 2009. QGIS geographic information system [software]. URL: http://qgis.org.

Rignot, E., Mouginot, J., Scheuchl, B., 2016. MEaSUREs Antarctic Grounding Line from Differential Satellite Radar Interferometry, Version 2. NASA National Snow and Ice Data Center Distributed Active Archive Center.

Roberts, J.L., Warner, R.C., Treverrow, A., 2013. Instruments and methods inferring ice-flow directions from single ice-sheet surface images using the radon transform. J. Glaciol. 59, 129–136. http://dx.doi.org/10.3189/2013JoG12J042, URL: https://www.cambridge.org/core.

Scambos, T., Fricker, H.A., Liu, C.-C., Bohlander, J., Fastook, J., Sargent, A., Massom, R., Wu, A.-M.M., 2009. Ice shelf disintegration by plate bending and hydro-fracture: Satellite observations and model results of the 2008 Wilkins ice shelf break-ups. Earth Planet. Sci. Lett. 280, 51–60. http://dx.doi.org/10.1016/j.epsl.2008.12.027, URL: www.nspo.org.

Shalom, S.R., Mandeville, G., 1982. Calculating minimum and maximum possible variances from n-tile grouped data. Qual. Quant. 16, 19–27, URL: https://link.springer.com/content/pdf/10.1007/BF00143817.pdf.

Stehman, S.V., 1997. Selecting and interpreting measures of thematic classification accuracy. Remote Sens. Environ. 62, 77–89. http://dx.doi.org/10.1016/S0034-4257(97)00083-7.

Sun, S., Cornford, S.L., Moore, J.C., Gladstone, R., Zhao, L., 2017. Ice shelf fracture parameterization in an ice sheet model. Cryosphere 11, 2543–2554. http://dx.doi.org/10.5194/tc-11-2543-2017, URL: https://www.the-cryosphere.net/11/2543/2017/.

Taha, A.A., Hanbury, A., 2015. SOFTWARE open access metrics for evaluating 3D medical image segmentation: analysis, selection, and tool. BMC Med. Imaging 15, 29. http://dx.doi.org/10.1186/s12880-015-0068-x, URL: www.visceral.eu.

Vaughan, D.G., Corr, H.F.J., Bindschadler, R.A., Dutrieux, P., Gudmundsson, G.H., Jenkins, A., Newman, T., Vornberger, P., Wingham, D.J., 2012. Subglacial melt channels and fracture in the floating part of pine island glacier, antarctica. J. Geophys. Res.: Earth Surf. 117, n/a–n/a. http://dx.doi.org/10.1029/2012JF002360, URL: http://doi.wiley.com/10.1029/2012JF002360.

Vieli, A., Payne, A.J., Shepherd, A., Du, Z., 2007. Causes of pre-collapse changes of the larsen B ice shelf: Numerical modelling and assimilation of satellite observations. Earth Planet. Sci. Lett. 259, 297–306. http://dx.doi.org/10.1016/j.epsl.2007.04.050.

Wang, S., Alexander, P., Wu, Q., Tedesco, M., Shu, S., 2021. Characterization of ice shelf fracture features using ICESat-2 – A case study over the Amery Ice Shelf. Remote Sens. Environ. 255, 112266. http://dx.doi.org/10.1016/j.rse.2020.112266.